Mechanics of Materials 117 (2018) 73–80

Contents lists available at ScienceDirect

Mechanics of Materials

journal homepage: www.elsevier.com/locate/mechmat

Research paper

A simple procedure to evaluate Cauchy stress tensor at the macro level based on computational micromechanics under general finite strain states

Néstor Darío Barulich[a,b], Luis Augusto Godoy[a,c,*], Patricia Mónica Dardati[b]

[a] Instituto de Estudios Avanzados en Ingeniería y Tecnología, IDIT UNC-CONICET, Avda. Vélez Sarsfield 1611, Ciudad Universitaria, X5016GCA Córdoba, Argentina
[b] Universidad Tecnológica Nacional, Facultad Regional Córdoba, Maestro M. López esq. Cruz Roja Argentina, X5016ZAA Córdoba, Argentina
[c] Universidad Nacional de Córdoba, FCEFyN, Avda. Vélez Sarsfield 1611, Ciudad Universitaria, X5016GCA Córdoba, Argentina

ARTICLE INFO

Keywords:
Multi-scale analysis
Finite elements
Finite strains
Homogenization
Micromechanics

ABSTRACT

This paper presents a new methodology to evaluate the Cauchy stress tensor at the macro level in computational micromechanics models. The use of control nodes to specify boundary conditions of a Representative Volume Element (RVE) allows deriving equations for the Cauchy stress components, with the consequence that numerical integration in the RVE is not performed. The proposed method allows use of computational micromechanics in commercial Finite Element software for a RVE subjected to general infinitesimal or finite strains. Because this methodology is obtained from the equivalence of power in the microscopic and macroscopic scales (Hill–Mandel principle) in a quasi-static problem, it is capable of dealing with micro-constituents under several constitutive laws. Numerical examples presented include simulations of elastic, hyper-elastic, and elasto-plastic fiber composite materials and a honeycomb microstructure. The present methodology can be used in multi-scale models to analyze non-linear structures made of heterogeneous materials.

1. Introduction

Multi-scale methods have proven to be useful techniques for modeling the loading process of structures made of heterogeneous materials (Nguyen et al., 2016). Such methods usually consider two scales with different characteristic lengths: In the smallest scale of analysis, known as the microscopic scale, the behavior of the heterogeneous microstructure is represented by explicitly simulating the interaction of components in a domain called Representative Volume Element (RVE). Boundary conditions have to be used not only to provide a way for the RVE to interact with the surrounding heterogeneous material but also to link microscopic and macroscopic kinematic relations (Nemat-Nasser and Hori, 1999). The structure is represented at the macroscopic scale, which is the largest scale of the analysis, whereas material behavior is obtained from the results at the microscopic scale.

Multi-scale approaches take advantage of numerical methods, such as the Finite Element Method (FEM), to simulate the evolution of complex microstructures under strain. *In-time* multi-scale schemes perform the calculations at the micro and the macro scales simultaneously (Nguyen et al., 2011), while *off-line* schemes collect results at the micro scale by solving a set of cases of interest, and then use these results for macroscopic scale simulations (Ghayour et al., 2016). Although the calculations for micro and macro scales are not carried out in the same sequence for both schemes, the general procedure at the microscopic scale used for *in-time* and *off-line* schemes is basically the same, and requires computation of the macroscopic stress tensor from an RVE boundary value problem for a given deformation state specified at the macroscopic scale.

Numerical integration algorithms are commonly used to obtain such stresses at the macroscopic scale for RVEs under infinitesimal or finite strains (see, for example, Barbero, 2013). The usual definition of the macroscopic Cauchy stress tensor $\boldsymbol{\sigma}$ at the macro scale as a function of the microscopic stress $\boldsymbol{\sigma}^m$ is given by

$$\sigma = \frac{1}{v}\int_v \sigma^m \, dv \tag{1}$$

in which v is the volume of the RVE in the deformed configuration. Numerical integration of Eq. (1) is performed using the stress tensor σ_{ij}^k at a Gauss integration point k and the corresponding weight factor for numerical integration v_k as

$$\sigma_{ij} = \frac{1}{v}\sum_{k=1}^{N} \sigma_{ij}^k v_k \tag{2}$$

Abadi (2010), Zahr-Viñuela and Pérez-Castellanos (2011), and Guo et al. (2014), among others, used Eq. (2) in their work, whereas Caporale et al. (2006), Barbero et al. (2013), and Barbero (2013)

* Corresponding author at: Universidad Nacional de Córdoba, FCEFyN, Avda. Vélez Sarsfield 1611, Ciudad Universitaria, X5016GCA Córdoba, Argentina.
E-mail address: luis.godoy@unc.edu.ar (L.A. Godoy).

http://dx.doi.org/10.1016/j.mechmat.2017.10.008
Received 17 February 2017; Received in revised form 7 October 2017; Accepted 12 October 2017
Available online 25 October 2017

employed a similar equation for infinitesimal strains. Although this is a well-established way to obtain the Cauchy stress tensor, it requires having data at every Gauss point, which is an amount of information that grows with the mesh size. To decrease this computational cost, some authors use a numerical approximation of the integral expressed at the RVE boundary (Caporale et al., 2006). Bonora and Rugiero (2006a, 2006b) and Rudykh and deBotton (2012) obtained a resultant force by averaging the forces at the boundary and then obtained a macroscopic stress by dividing such resultant by an area.

Some authors proposed methods in which the stresses at macroscopic scale are obtained in a post-process procedure embedded in the boundary value problem of the RVE. Michel et al. (1999) assigned the macroscopic strain to the degree of freedom of an additional node on each finite element at microscopic scale. Then, in the complete Finite Element model in such small scale, the assembled force vector contains the macroscopic stresses. This method was applied by Daxner et al. (2006), Rasool and Böhm (2012), and Böhm and Rasool (2016). van Dijk (2016) presented a method in which macroscopic stresses arise as macroscopic strain reactions; such formulation used Lagrange multipliers, periodic boundary condition, and was based on the Hill–Mandel principle. These methods (Michel et al., 1999; van Dijk, 2016) need for special Finite Element software and often this constitutes a disadvantage.

Other authors employ three additional nodes, known as control nodes, to obtain the Cauchy stress. Control nodes are often used to implement the boundary conditions and the associated forces divided by the transverse deformed area have been interpreted as macroscopic Cauchy stresses (Zahr-Viñuela and Pérez-Castellanos, 2011). This same idea has been used to obtain the behavior of a homogenized shell employing forces and moments per unit length as macroscopic quantities (Adolfsson and Gudmundson, 1997; Piezel et al., 2012). Rather than postulate an equation for the macroscopic stress based on intuition, Li and Wongsto (2004) obtained a set of equations in terms of the forces at control nodes to compute the stress component corresponding to uniaxial or shear strain states. A similar approach based on the equivalence of energy between microscopic and macroscopic scales has been proposed by Sun and Vaidya (1996) under infinitesimal strains, and by Barulich et al. (2016) for simple shear and uniaxial strain cases under finite strains.

This paper presents a new methodology (hereafter designated as MCT for Methodology for Complete Tensor) to calculate the complete Cauchy stress tensor for RVEs subjected to general infinitesimal or finite strain states. This methodology does not need to perform numerical integrations, thus avoiding complexity during its implementation. The developed equations are based on the Hill–Mandel principle and can be implemented in general purpose Finite Element software. The methodology presented can deal with quasi-static RVE problems including geometric and/or material non-linear behavior.

This work is organized as follows: In the next section the unit cells and periodic boundary conditions are detailed; then, the formulation of MCT is presented showing that it is a general technique that comprises results available in the literature for specific strain states. Numerical examples are presented to illustrate the procedure and verify the methodology.

2. Post-processing methodology

2.1. Geometry of unit cells considered

Three types of unit cells (UC), illustrated in Fig. 1, were used in this paper: A prism having a parallelogram with equal sides at the base; a truncated octahedron; and a hollow hexagonal prism. The first two UC were used here to represent a periodic fiber reinforced composite material, while the hollow hexagonal prism represents a honeycomb microstructure (van Dijk, 2016).

In order to simulate a material with periodic microstructure, periodicity vectors were employed as explained by Oller et al. (2005). The periodicity vectors used for prism and truncated octahedron UCs are described in Barulich et al. (2016), while those for the honeycomb UC are shown in Fig. 2 and can be expressed as

$$\begin{aligned}\mathbf{P_1} &= \tfrac{3}{2} l_e\, \mathbf{i} \;-\; a\, \mathbf{j} \\ \mathbf{P_2} &= \tfrac{3}{2} l_e\, \mathbf{i} \;+\; a\, \mathbf{j} \\ \mathbf{P_3} &= h\, \mathbf{k}\end{aligned} \tag{3}$$

where the UC dimensions are

$$a = \frac{6\, t_w + \sqrt{36\, {t_w}^2 - 36\, V_{fo}\, {t_w}^2 + 36\, V_{fo}\, r^2 - 6\, V_{fo} \sqrt{3}\, \pi\, r^2}}{6\, V_{fo}} \tag{4}$$

$$l_e = \frac{2a}{3}\sqrt{3} \tag{5}$$

In these equations, the values of the apothem a and the side length l_e are obtained from the assumed values of the half wall thickness t_w, the inner radius r, and the honeycomb volume fraction V_{fo}. Notice that the UC height h, shown in Fig. 2, is independent of other dimensions.

2.2. Periodic boundary conditions under finite strains

The methodology presented in this article makes use of forces and displacements at control nodes; therefore, in order to explain this technique, periodic boundary conditions employing control nodes are next given in detail, although they have been recently reported in the literature (see for example Zahr-Viñuela and Pérez-Castellanos, 2011; Barulich et al., 2016).

To express the periodic boundary conditions it is useful to employ the concept of "corresponding points" (see Zahr-Viñuela and Pérez-Castellanos, 2011), which implies that the subtraction of the position $\mathbf{X}^+$ and $\mathbf{X}^-$ of two corresponding points gives a linear combination of the periodicity vectors with integer coefficients, $\mathbf{P_v}$:

$$\mathbf{P_v} = \mathbf{X}^+ - \mathbf{X}^- \tag{6}$$

Periodic boundary conditions involve relations between traction vectors $\mathbf{t}^+$ and $\mathbf{t}^-$ at every pair of corresponding points in the UC boundary (Guo et al., 2007, 2014):

$$\mathbf{t}^+ = -\mathbf{t}^- \tag{7}$$

and relations between positions $\mathbf{x}^+$ and $\mathbf{x}^-$ of such corresponding points in the deformed configuration

$$\mathbf{x}^+ - \mathbf{x}^- = \mathbf{F}(\mathbf{X}^+ - \mathbf{X}^-) \tag{8}$$

where $\mathbf{F}$ is the known macroscopic deformation gradient tensor which is to be imposed at UC. The expression linking $\mathbf{F}$ and the macroscopic displacement gradient $\nabla\mathbf{U}$ in the reference configuration is (Holzapfel, 2000)

$$\mathbf{F} = \nabla\mathbf{U} + \mathbf{I} \tag{9}$$

where $\mathbf{I}$ is the identity tensor and the components of operator ∇ are

$$[\nabla(\cdot)]_{ij} = \frac{\partial(\cdot)_i}{\partial X_j} \tag{10}$$

Using (9) and (6), the Eq. (8) can be expressed in terms of displacements of corresponding nodes $\mathbf{u}^+$ and $\mathbf{u}^-$ as

$$\mathbf{u}^+ - \mathbf{u}^- = \nabla\mathbf{U}\,\mathbf{P_v} \tag{11}$$

In this work, conditions (11) were implemented by means of multipoint linear constraints (using *EQUATION command in software ABAQUS, 2009) writing equations in the form

$$u_i{}^+ - u_i{}^- - \frac{1}{\alpha} u_{i1} P_{vx} - \frac{1}{\alpha} u_{i2} P_{vy} - \frac{1}{\alpha} u_{i3} P_{vz} = 0 \tag{12}$$

where $i = 1, 2, 3$; u_{ij} are the displacement components in direction i of control node j. Three control nodes were added in this work in order to

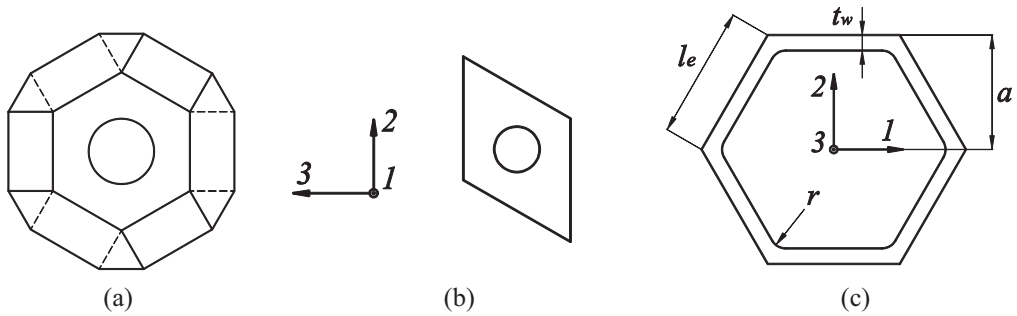

Fig. 1. Front view of unit cells: (a) truncated octahedron; (b) prism; (c) hollow hexagonal prism.

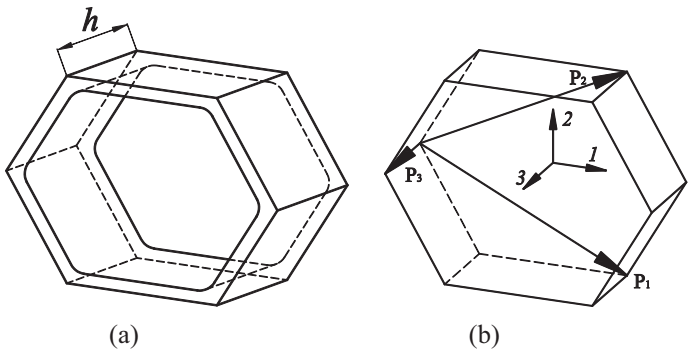

Fig. 2. Hollow hexagonal prism as unit cell for the honeycomb microstructure: (a) perspective of the UC; (b) external boundary of UC with periodicity vectors.

get nine additional degrees of freedom (DOF). Then, the components of the macroscopic displacement gradient are used to impose such DOF as:

$$u_{ij} = \alpha[\nabla \mathbf{U}]_{ij} \tag{13}$$

Dimensional consistency in Eqs. (12) and (13) is achieved using a unit factor α with length units.

When using linear multi-point constrains, equations for each pair of corresponding points should be carefully selected, as was pointed out by Barbero (2013), among others. For the honeycomb unit cell, a possible set of equations of type (12) can be obtained from Tables 1 to 3 in which the first and second DOF in such equation are shown for each face, edge and vertices pair, together with the corresponding $\mathbf{P_v}$ vector. Fig. 3 shows identification of faces, edges and vertices. Eqs. (12) for the truncated octahedron and prismatic unit cells have been published by Barulich et al. (2016).

2.3. Evaluation of stress tensor at macro level

2.3.1. Internal mechanical power

Under a given macroscopic strain state, a stress field is induced at a RVE. The stress power, or rate of internal mechanical work, identified as $P_{int}(t)$, is a scalar associated with the stress field acting on the RVE in the reference configuration V at time t. Following Holzapfel (2000), P_{int} is given by

$$P_{int}(t) = \int_V \mathbf{P}^m : \dot{\mathbf{F}}^m dV \tag{14}$$

where $\mathbf{P}^m$ is the first Piola–Kirchhoff stress tensor; and $\dot{\mathbf{F}}^m$ is the rate of deformation gradient $\mathbf{F}^m$ at microscopic scale. Units of $P_{int}(t)$ are work per time unit.

Table 1
$\mathbf{P_v}$ vectors of different pairs of faces for honeycomb UC.

1st DOF	2nd DOF	P_v
Fr	Po	**P3**
S	I	**P2–P1**
RI	LS	**P1**
RS	LI	**P2**

Table 2
$\mathbf{P_v}$ vectors of different pairs of edges for honeycomb UC.

1st DOF	2nd DOF	P_v	1st DOF	2nd DOF	P_v
E3	E1	**P2–P1**	E10	E9	**P3**
E2	E1	**P3**	E11	E9	**P1**
E4	E1	**P2–P1 + P3**	E12	E9	**P1 + P3**
E6	E5	**P3**	E14	E13	**P2**
E7	E5	**P2**	E15	E13	**P1**
E8	E5	**P2 + P3**	E17	E16	**P2–P1**
			E18	E16	**P2**

Table 3
$\mathbf{P_v}$ vectors of different pairs of vertices for honeycomb UC.

1st DOF	2nd DOF	P_v	1st DOF	2nd DOF	P_v
V2	V1	**P2**	V8	V7	**P2**
V3	V1	**P1**	V9	V7	**P3**
V4	V1	**P3**	V10	V7	**P2–P1**
V5	V1	**P2 + P3**	V11	V7	**P2 + P3**
V6	V1	**P1 + P3**	V12	V7	**P2–P1 + P3**

The first Piola–Kirchhoff stress tensor satisfies the condition

$$\mathbf{P} = J\sigma(\mathbf{F}^{-1})^T \tag{15}$$

where $J = det(\mathbf{F})$ is the Jacobian of $\mathbf{F}$. Next, consider

$$\dot{\mathbf{F}} = \nabla(\mathbf{V}_{RC}(\mathbf{X}, t)) \tag{16}$$

where $\mathbf{V}_{RC}$ is the velocity and is written in terms of reference configuration $\mathbf{X}$ at a time t.

For an RVE, the Hill–Mandel condition may be written as given by de Souza Neto and Feijóo (2008)

$$\mathbf{P}: \dot{\mathbf{F}} = \frac{1}{V}\int_V \mathbf{P}^m : \dot{\mathbf{F}}^m dV \tag{17}$$

where $\mathbf{P}^m$ and $\mathbf{P}$ are the first Piola–Kirchhoff stress tensor at the micro and the macro scales, respectively; $\dot{\mathbf{F}}^m$ and $\dot{\mathbf{F}}$ are the rates of

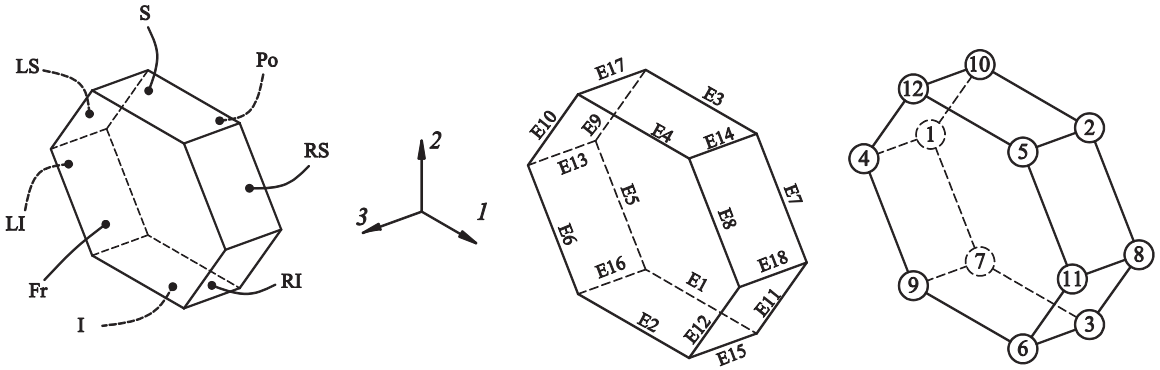

Fig. 3. Identifications of faces edges and vertices in the honeycomb UC.

deformation gradient again at micro and macro scales. Body force and inertia have not been included in this work, but these effects have been taken into account by de Souza Neto et al. (2015).

Thus, the stress power results in

$$P_{int}(t) = V\ \mathbf{P}\colon \dot{\mathbf{F}} \tag{18}$$

or

$$\begin{aligned} P_{int}(t) \;=\; & V\,(P_{11}\dot{F}_{11} + P_{12}\dot{F}_{12} + P_{13}\dot{F}_{13}+\ldots \\ & + P_{21}\dot{F}_{21} + P_{22}\dot{F}_{22} + P_{23}\dot{F}_{23}+\ldots \\ & + P_{31}\dot{F}_{31} + P_{32}\dot{F}_{32} + P_{33}\dot{F}_{33}) \end{aligned} \tag{19}$$

2.3.2. External mechanical power

In a domain of volume V undergoing deformation, the external mechanical power $P_{ext}(t)$ is defined as the power due to external forces at time t. If the kinetic energy change in the domain V is zero, then the problem may be classified as quasi-static, in which the variables may still be time-dependent. Therefore, the energy balance (see Holzapfel, 2000, Eq. (4.102)) results in

$$P_{ext}(t) = P_{int}(t) \tag{20}$$

In a finite element model of a RVE with control nodes, external work is only done through forces acting on such control nodes. Thus, the external power is the summation of products between forces and velocities in the direction of each force. For a general strain state $P_{ext}(t)$ can be written as

$$\begin{aligned} P_{ext}(t) \;=\; & R_{11}\dot{u}_{11} + R_{12}\dot{u}_{12} + R_{13}\dot{u}_{13}+\ldots \\ & + R_{21}\dot{u}_{21} + R_{22}\dot{u}_{22} + R_{23}\dot{u}_{23}+\ldots \\ & + R_{31}\dot{u}_{31} + R_{32}\dot{u}_{32} + R_{33}\dot{u}_{33} \end{aligned} \tag{21}$$

where R_{ij} and $\dot{u}_{ij}$ are the force and velocity in direction i at control node j, respectively. Considering boundary conditions (13) and Eq. (9), $\dot{u}_{ij}$ can be expressed as

$$\dot{u}_{ij} = \alpha\dot{F}_{ij} \tag{22}$$

then, P_{ext} takes the form

$$\begin{aligned} P_{ext}(t) \;=\; & \alpha(R_{11}\dot{F}_{11} + R_{12}\dot{F}_{12} + R_{13}\dot{F}_{13}+\ldots \\ & + R_{21}\dot{F}_{21} + R_{22}\dot{F}_{22} + R_{23}\dot{F}_{23}+\ldots \\ & + R_{31}\dot{F}_{31} + R_{32}\dot{F}_{32} + R_{33}\dot{F}_{33}) \end{aligned} \tag{23}$$

2.3.3. Equation for the macroscopic Cauchy stress tensor

Taking into account the expressions for the internal and external power in Eqs. (23) and (19), the energy balance, Eq. (20), can be derived respect to $\dot{F}_{ij}$ giving

$$\alpha R_{ij} = V\,P_{ij} \tag{24}$$

as a consequence, the first Piola–Kirchhoff stress tensor $\mathbf{P}$ can be obtained as

$$P_{ij} = \frac{\alpha R_{ij}}{V} \tag{25}$$

Following Eq. (3.9) in Holzapfel (2000)

$$\sigma = J^{-1}\mathbf{P}\mathbf{F}^{T} \tag{26}$$

an expression to evaluate the macroscopic Cauchy stress tensor is obtained:

$$\sigma_{ij} = J^{-1}F_{jk}\frac{\alpha R_{ik}}{V} \tag{27}$$

The Eq. (27) holds for a general finite strain state in quasi-static problems and it is expressed as a function of the forces at control nodes and the deformation gradient at time t.

Specific deformation states give particular and useful forms of the last equation. In the following, reduced forms of (27) are presented for specific deformation states. When the deformation gradient has the principal stretches λ_i in its diagonal, the Eq. (27) reduces to

$$[\sigma] = \frac{\alpha}{J\,V}\begin{bmatrix} R_{11}\lambda_1 & R_{12}\lambda_2 & R_{13}\lambda_3 \\ R_{21}\lambda_1 & R_{22}\lambda_2 & R_{23}\lambda_3 \\ R_{31}\lambda_1 & R_{32}\lambda_2 & R_{33}\lambda_3 \end{bmatrix} \tag{28}$$

with $J = \lambda_1\,\lambda_2\,\lambda_3$. If a deformation gradient corresponding to a simple shear state is imposed on the RVE, with a unique varying component F_{21}, then $J = 1$ and the Eq. (27) takes the form

$$[\sigma] = \frac{\alpha}{V}\begin{bmatrix} R_{11} & R_{11}F_{21} + R_{12} & R_{13} \\ R_{21} & R_{21}F_{21} + R_{22} & R_{23} \\ R_{31} & R_{31}F_{21} + R_{32} & R_{33} \end{bmatrix} \tag{29}$$

The results for the components in the diagonal of (28) and the component σ_{21} in Eq. (29) coincide with the formulas presented by Barulich et al. (2016) for uniaxial and simple shear cases but here, Eqs. (28) and (29), allow obtaining the complete stress tensor for such deformation states.

A pure shear deformation state includes a deformation gradient such as

$$\mathbf{F} = \begin{bmatrix} 1 & F_{12} & 0 \\ F_{21} & 1 & 0 \\ 0 & 0 & 1 \end{bmatrix} \tag{30}$$

which makes (27) reduce to

$$[\sigma] = \frac{\alpha}{J\,V}\begin{bmatrix} R_{11} + R_{12}F_{12} & R_{11}F_{21} + R_{12} & R_{13} \\ R_{21} + R_{22}F_{12} & R_{21}F_{21} + R_{22} & R_{23} \\ R_{31} + R_{32}F_{12} & R_{31}F_{21} + R_{32} & R_{33} \end{bmatrix} \tag{31}$$

where the Jacobian of $\mathbf{F}$ is $J = 1 - F_{12}F_{21}$.

For small strains the deformation gradient $\mathbf{F}$ tends to identity and its Jacobian J tends to unity, therefore (27) reduces to

$$\sigma_{ij} = \frac{\alpha R_{ij}}{V} \tag{32}$$

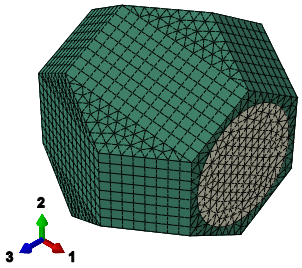

Fig. 4. Finite Element mesh with 15,974 quadratic elements for the truncated octahedral UC.

Li and Wongsto (2004) reported similar scalar formulas to obtain the Cauchy stress components related to uniaxial stress or shear states, while in this work, the Eq. (32) holds for any small strain state. Notice that any other specific equation for the Cauchy stress tensor can be derived from (27) by using the corresponding deformation gradient.

The methodology to evaluate the Cauchy stress tensor, presented in this work, can be summarized as follows: (i) Obtain the reaction forces R_{ij} at control nodes by solving the FEM problem at the micro level for a given macroscopic deformation gradient **F**, (ii) Use general Eq. (27) or particular Eqs. (28), (29), (31) or (32) depending on the applied strain state to compute the Cauchy stress tensor.

This procedure does not require performing numerical integration, and an important consequence is that less complexity in implementation and less information and computer time are needed during the post-process. Because the method is based on mechanical energy balance in quasi-static problems, the range of application includes material or kinematic nonlinearities. Further, the methodology is not only appropriate for PBC but also for any boundary condition that could be implemented by means of control nodes.

3. Results

In this section, the MCT is validated by means of comparisons with a procedure using numerical integration. The simulations were done using the general purpose finite element program ABAQUS (2009).

3.1. Linear elastic composite

Barbero presented two examples (see Sections 6.2 and 6.3 in Barbero, 2013), in which the elastic properties of a composite lamina are obtained using computational micromechanics; these results are next used to verify the MCT in an elastic small-strain problem. The strategy in this section is to reconstruct the macroscopic elastic constitutive matrix employing results reported by Barbero, to apply a given small strain state, selected in this work for this particular example, and to compare the obtained stresses with the results of MCT through Eqs. (32).

The composite material includes elastic carbon fibers with Young modulus $E_f = 241$ GPa, Poisson ratio $\nu_f = 0.2$, and elastic epoxy matrix with $E_m = 3.12$ GPa and $\nu_m = 0.38$. The fibers have a hexagonal fiber arrangement, which makes the macroscopic material to be transversely isotropic. The fiber volume fraction is $V_f = 40\%$ and the results for the elastic constants computed by Barbero (2013) are: $G_{12} = 2{,}579$ MPa, $E_1 = 98{,}197$ MPa, $E_2 = 7{,}472$ MPa, $\nu_{12} = 0.299$, $\nu_{23} = 0.540$. The corresponding compliance matrix is given by

$$[S] = \begin{bmatrix} \frac{1}{E_1} & -\frac{\nu_{12}}{E_1} & -\frac{\nu_{12}}{E_1} & 0 & 0 & 0 \\ -\frac{\nu_{12}}{E_1} & \frac{1}{E_2} & -\frac{\nu_{23}}{E_2} & 0 & 0 & 0 \\ -\frac{\nu_{12}}{E_1} & -\frac{\nu_{23}}{E_2} & \frac{1}{E_2} & 0 & 0 & 0 \\ 0 & 0 & 0 & \frac{E_2}{2(1+\nu_{23})} & 0 & 0 \\ 0 & 0 & 0 & 0 & \frac{1}{G_{12}} & 0 \\ 0 & 0 & 0 & 0 & 0 & \frac{1}{G_{12}} \end{bmatrix} \tag{33}$$

The Cauchy stress in vector form $\{\sigma\}$ is obtained as

$$\{\sigma\} = [C]\{\varepsilon\} \tag{34}$$

where the stiffness matrix is $[C] = [S]^{-1}$. The strains are given in the form

$$\{\varepsilon\} = \{\varepsilon_{11}\ \varepsilon_{22}\ \varepsilon_{33}\ \gamma_{23}\ \gamma_{13}\ \gamma_{12}\}^{\mathrm{T}} \tag{35}$$

As an illustrative example, the applied strain is $\{\varepsilon\} = \{6\ -7\ -4\ 5\ 8\ -6\}^{\mathrm{T}} \times 10^{-5}$. Notice that $\{\varepsilon\}$ is an arbitrary small strain vector, and it was selected here to obtain non-zero Cauchy stress components in the composite. Barbero used a UC with a parallelepiped shape; here, a truncated octahedra was employed as a UC with up to 16,000 quadratic finite elements (Fig. 4). Tetrahedral and wedge-shaped Finite Elements were selected given that they easily generate a periodic mesh for this UC. Results for the Cauchy stress tensor obtained with Eqs. (34) with elastic constants taken from Barbero (2013) and Eq. (32) of the MCT, for two meshes with a number of elements N_{el}, are given in Table 4 and they show a good agreement. This example also shows that the presented methodology, without modification, is capable to analyze UCs with non-conventional shapes, such as the truncated octahedra.

3.2. Elastic–plastic composite

This section shows the results for the Cauchy stress tensor obtained by means of Eq. (32) and numerical integration in an elastic–perfectly plastic fiber composite under small strains. Fiber and matrix properties are $E^m = E^f = 100$ GPa, $\nu^m = \nu^f = 0.25$ for the Young moduli and Poisson ratios; von Mises plasticity with an associative rule were used, with yield stresses $\sigma_0^m = 100$ MPa and $\sigma_0^f = 500$ MPa. Fiber volume fraction of 56.25% was assumed in a prismatic UC with a hexagonal arrangement. The imposed macroscopic deformation gradient is

$$\mathbf{F} = \begin{bmatrix} F_{11} & 0 & 0 \\ 0.001 & 0.999 & 0 \\ 0.0005 & -0.001 & 1.001 \end{bmatrix} \tag{36}$$

where F_{11} is obtained from the numerical solution of the UC problem such as $P_{11} = 0$; this zero value is obtained by imposing no displacement on the first DOF in control node 1 which implies zero reaction force ($R_{11} = 0$) and, following Eq. (25), $P_{11} = 0$ is obtained. The deformation gradient for this example was chosen to initiate the plastic flow and to reach a plateau in the Cauchy stress components, and also to generate different values among such components. Two meshes were used in this example with 7570 and 19,430 quadratic wedge-shaped elements providing an accurate representation of the fiber and matrix behavior while conforming a periodic mesh in the UC. The maximum differences among stresses obtained with those meshes are smaller than

Table 4
Cauchy stress components [MPa] in a transversely isotropic linear elastic CFRP under a three-axial small strain state.

	σ_{11}	σ_{22}	σ_{33}	σ_{23}	σ_{13}	σ_{12}
MCT Eq. (32), $N_{el} = 1{,}984$	5.527	−0.694	−0.549	0.121	0.207	−0.155
MCT Eq. (32), $N_{el} = 15{,}974$	5.527	−0.695	−0.549	0.121	0.207	−0.155
Eq. (34)	5.521	−0.693	−0.548	0.121	0.206	−0.155

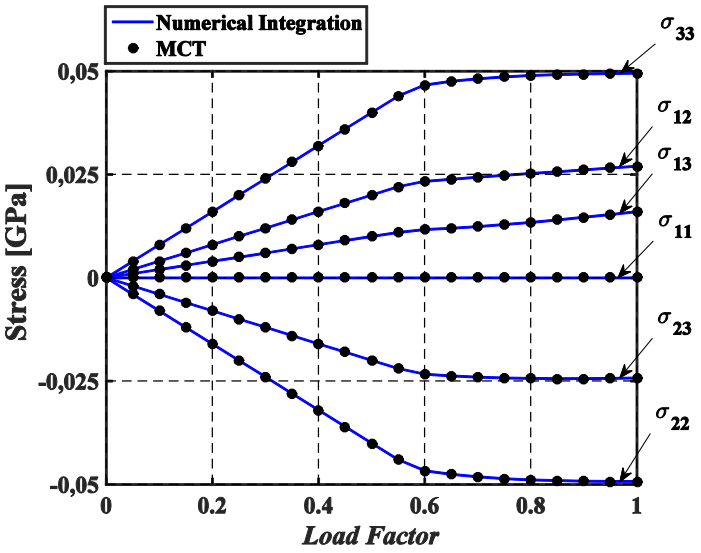

Fig. 5. Cauchy stress components for an elastic–plastic composite: Comparison between the present method (MCT) and numerical integration, Eq. (2).

0.06% with respect to the maximum value obtained for the σ_{33}, showing convergence has been reached.

Results for the Cauchy stress components obtained by the methodology presented in this paper (MCT) and numerical integration through Eq. (2) are shown in Fig. 5 as a function of a load factor; when such load factor is zero, the deformation gradient **F** is equal to identity tensor, while if the load factor is equal to unity, the deformation gradient **F** will be given by (36). It can be seen that results are very similar showing the good performance of MCT for elastic-plastic problems under small strains.

3.3. Hyper-elastic composite

In this section, the MCT has been applied to a composite with continuous fibers in hexagonal configuration (prismatic UC), having $V_f = 50\%$. Isotropic hyper-elastic incompressible behavior is assumed for fiber and matrix; a Neo-Hookean model was assumed for the fibers whose strain energy density W is given by

$$W = C_{10}(I_1 - 3) \tag{37}$$

where C_{10} is a material parameter and the first invariant I_1 is defined as

$$I_1 = \mathrm{tr}(\mathbf{F}^T\mathbf{F}) \tag{38}$$

An Ogden model was used for the matrix and its strain energy density W is

$$W = \sum_{i=1}^{N} \frac{2\mu_i}{\alpha_i^2}[\lambda_1^{\alpha_i} + \lambda_2^{\alpha_i} + \lambda_3^{\alpha_i} - 3] \tag{39}$$

where μ_i and α_i are material parameters; N is the number of terms used in the model; λ_i are the principal stretching of the deformation gradient acting in the material. The initial shear modulus for the assumed Neo-Hookean material is given by

$$\mu_0^f = 2C_{10} \tag{40}$$

while for the Ogden material, the initial shear modulus is

$$\mu_0^m = \sum_{i=1}^{N} \mu_i \tag{41}$$

The material parameters assumed for the Ogden material are $\mu_1 = 630\,\mathrm{kPa}$, $\mu_2 = 1.2\,\mathrm{kPa}$, $\mu_3 = -10\,\mathrm{kPa}$, $\alpha_1 = 1.3$, $\alpha_2 = 5$, $\alpha_3 = -2$ and, for the Neo-Hookean material, $C_{10} = 2.1125\,\mathrm{MPa}$. The ratio of initial shear moduli of fiber and matrix is 6.8.

Since the applied deformation gradient can have arbitrary values, the following **F** was chosen so that the Cauchy stress components have different values among them

$$\mathbf{F} = \begin{bmatrix} 2 & 0 & 0 \\ 1 & F_{22} & 0 \\ -1 & -0.7 & 1 \end{bmatrix} \tag{42}$$

in which F_{22} is obtained from the numerical solution of the UC such as $P_{22} = 0$. The general Eq. (27) was used to evaluate Cauchy stress. A mesh with 420 linear wedge-shaped elements was used in a hybrid formulation. Such formulation is appropriate for modeling incompressible materials. The mesh provides a good approximation of the composite behavior since, when the amount of elements was increased up to 762, the model showed changes smaller than 0.7% with respect to the maximum value for σ_{11}. Results of the present post-processing method are compared in Fig. 6 with those obtained by numerical integration, Eq. (2), and excellent agreement is found between them.

3.4. Hyper-elastic honeycomb microstructure

A honeycomb microstructure made of a hyper-elastic material is considered in this section to show that MCT can be used to compute stresses in microstructures with large changes in shape. The Finite Element mesh is shown in Fig. 7 and it has 4200 hybrid formulation brick elements having quadratic shape functions and 20 nodes (C3D20H, in ABAQUS nomenclature). The mesh shown in Fig. 7 is an adequate discretization for the microstructure since a more refined mesh with 9060 elements led to differences in stress components that did not exceed 0.01% with respect to the maximum compressive value obtained for σ_{22} with the finer mesh. The inner edges have a fillet radius r equal to half the wall thickness $t_w = 1\ \mathrm{m}^{-6}$ and the honeycomb volume fraction is $V_{fo} = 15\%$; the height h was chosen for the model to have a unique layer of elements in the direction 3. The material is incompressible of Neo-Hookean type with $C_{10} = 2.1125\,\mathrm{MPa}$. The microstructure is compressed in the direction of the axis 1 with a deformation gradient given by

$$\mathbf{F} = \begin{bmatrix} 0.5 & 0 & 0 \\ 0 & 1 & 0 \\ 0 & 0 & 1 \end{bmatrix} \tag{43}$$

This compressive deformation gradient was chosen because it causes an unstable behavior of the microstructure with notable changes in shape (van Dijk, 2016).

Fig. 8 shows the values for the Cauchy stress components for the MCT and numerical integration, Eq. (2), and they are in good

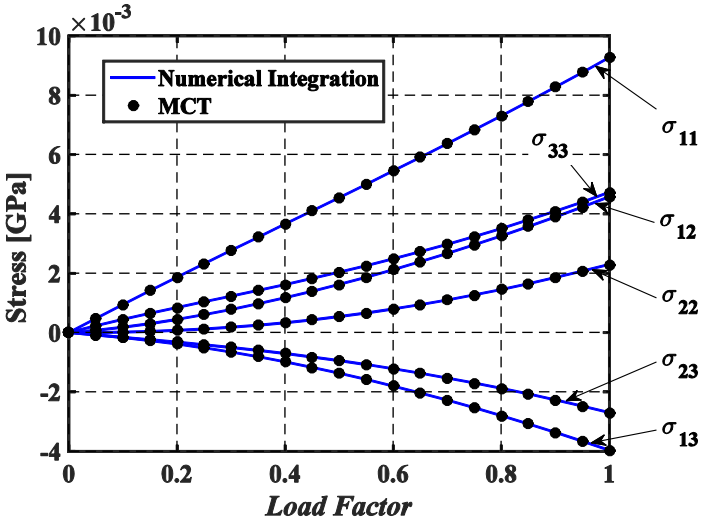

Fig. 6. Cauchy stress for a hyper-elastic composite with hexagonal fiber arrangement: Comparison between the present method (MCT) and numerical integration, Eq. (2).

agreement. In Eq. (27), it is important to use the complete volume of the initial configuration V which is equal to the volume of the material plus the hollow part of the unit cell. Finally, in Fig. 9a quarter of the UC is shown in the initial and deformed states corresponding to $F_{11} = 0.75$ and $F_{11} = 0.5$. The Cauchy stress component σ_{11} is also shown in the UC domain. The trends of the stress curves and deformed states are similar to the ones reported by van Dijk (2016).

4. Conclusions

A new methodology for calculation of the Cauchy stress tensor at the macroscopic level in computational micro-mechanics models has been presented in this work. The formulation accounts for general strain states and it is restricted to quasi-static problems. Numerical integration at the microscopic domain is not performed in the present approach; thus, the methodology avoids complexities in implementation and uses less information than numerically integrated approaches. Because the present formulation is derived from the Hill–Mandel principle, the approach may also be employed for other boundary conditions which could be implemented by means of control nodes.

Verification has been presented by comparison with numerical integration in a truncated octahedron, prismatic, and honeycomb

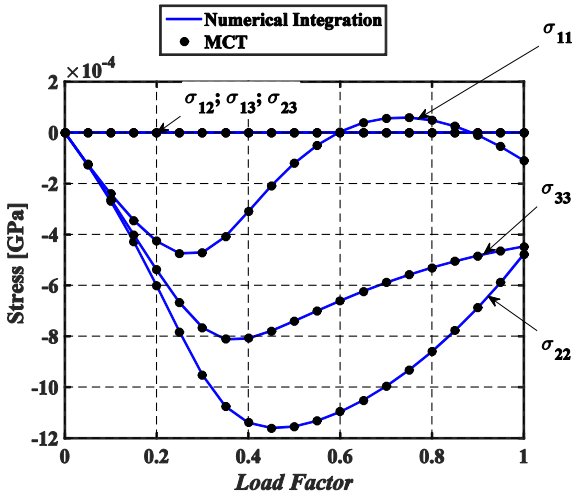

Fig. 8. Cauchy stress for a hyper-elastic honeycomb microstructure: Comparison between the present method (MCT) and numerical integration of Eq. (2).

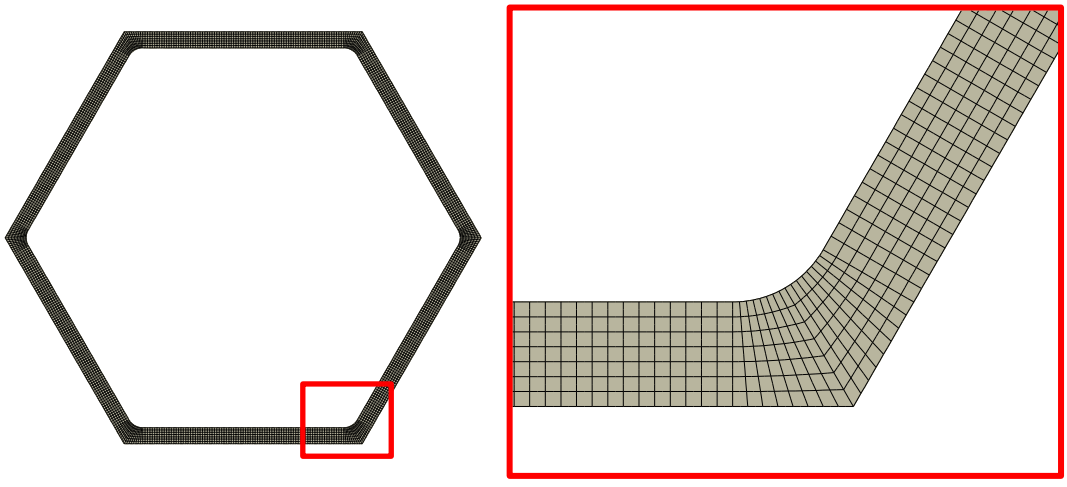

Fig. 7. (a) Finite Element mesh for the honeycomb microstructure. (b) Detail in a corner of the unit cell.

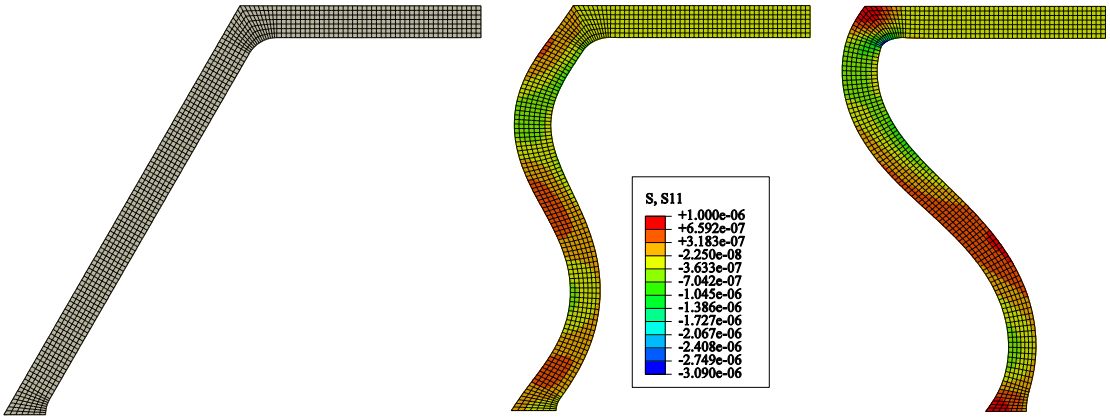

Fig. 9. Hyper-elastic honeycomb microstructure. (a) Quarter of the mesh. (b) Cauchy stress component σ_{11} [10^{-3} GPa] in the deformed state for $F_{11} = 0.75$. (c) Cauchy stress σ_{11} for $F_{11} = 0.5$.

microscopic domains; cases consider elastic, elastic-plastic, and hyper-elastic materials models at microscopic scale. Moreover, it is shown that the developed general equations can reproduce specific results already presented in the literature for uniaxial and shear cases under small or finite strains, thus showing that this methodology is a general one.

Finally, the present approach is a good candidate for multi-scale in-time simulations, in which the calculations at the micro and macro level are performed simultaneously.

Acknowledgments

NDB and LAG were supported by CONICET, the Science Research Council of Argentina during this research. The authors thank the support received from grants of CONICET (PIP 0126), SECyT-UNC, Ministerio de Ciencia y Tecnología de la Prov. de Cordoba, and UTN-FRC (UTI 2119).

References

Abadi, M.T., 2010. Characterization of heterogeneous materials under shear loading at finite strain. Compos. Struct. 92 (2), 578–584. http://dx.doi.org/10.1016/j.compstruct.2009.09.002.

Abaqus v. 6.7, 2009. Dassault Systèmes, Providence, RI, USA.

Adolfsson, E., Gudmundson, P., 1997. Thermoelastic properties in combined bending and extension of thin composite laminates with transverse matrix cracks. Int. J. Solids Struct. 34 (16), 2035–2060. http://dx.doi.org/10.1016/S0020-7683(96)00156-4.

Barbero, E.J., 2013. Finite Element Analysis of Composite Materials Using Abaqus TM. CRC Press, Boca Raton, FL.

Barbero, E.J., Cosso, F.A., Campo, F.A., 2013. Benchmark solution for degradation of elastic properties due to transverse matrix cracking in laminated composites. Compos. Struct. 98, 242–252. http://dx.doi.org/10.1016/j.compstruct.2012.11.009.

Barulich, N.D., Godoy, L.A., Dardati, P.M., 2016. Evaluation of stresses at the macro level based on computational micromechanics under finite strains. Mech. Mater. 101, 93–101. http://dx.doi.org/10.1016/j.mechmat.2016.07.006.

Böhm, H.J., Rasool, A., 2016. Effects of particle shape on the thermoelastoplastic behavior of particle reinforced composites. Int. J. Solids Struct. 87, 90–101. http://dx.doi.org/10.1016/j.ijsolstr.2016.02.028.

Bonora, N., Ruggiero, A., 2006a. Micromechanical modeling of composites with mechanical interface—part 1: unit cell model development and manufacturing process effects. Compos. Sci. Technol. 66 (2), 314–322. http://dx.doi.org/10.1016/j.compscitech.2005.04.041.

Bonora, N., Ruggiero, A., 2006b. Micromechanical modeling of composites with mechanical interface—part II: damage mechanics assessment. Compos. Sci. Technol. 66 (2), 323–332. http://dx.doi.org/10.1016/j.compscitech.2005.04.043.

Caporale, A., Luciano, R., Sacco, E., 2006. Micromechanical analysis of interfacial debonding in unidirectional fiber-reinforced composites. Comput. Struct. 84 (31), 2200–2211. http://dx.doi.org/10.1016/j.compstruc.2006.08.023.

Daxner, T., Bitsche, R.D., Böhm, H.J., 2006. Space-filling polyhedra as mechanical models for solidified dry foams. Mater. Trans. 47 (9), 2213–2218. http://dx.doi.org/10.2320/matertrans.47.2213.

de Souza Neto, E.A., Blanco, P.J., Sánchez, P.J., Feijóo, R.A., 2015. An RVE-based multiscale theory of solids with micro-scale inertia and body force effects. Mech. Mater. 80, 136–144. http://dx.doi.org/10.1016/j.mechmat.2014.10.007.

de Souza Neto, E.A., Feijóo, R.A., 2008. On the equivalence between spatial and material volume averaging of stress in large strain multi-scale solid constitutive models. Mech. Mater. 40 (10), 803–811. http://dx.doi.org/10.1016/j.mechmat.2008.04.006.

Ghayour, M., Hosseini-Toudeshky, H., Jalalvand, M., Barbero, E.J., 2016. Micro/macro approach for prediction of matrix cracking evolution in laminated composites. J. Compos. Mater. 50 (19), 2647–2659. http://dx.doi.org/10.1177/0021998315610179.

Guo, Z., Peng, X., Moran, B., 2007. Large deformation response of a hyperelastic fibre reinforced composite: theoretical model and numerical validation. Compos. Part A: Appl. Sci. Manufact. 38 (8), 1842–1851. http://dx.doi.org/10.1016/j.compositesa.2007.04.004.

Guo, Z., Shi, X., Chen, Y., Chen, H., Peng, X., Harrison, P., 2014. Mechanical modeling of incompressible particle-reinforced neo-Hookean composites based on numerical homogenization. Mech. Mater. 70, 1–17. http://dx.doi.org/10.1016/j.mechmat.2013.11.004.

Holzapfel, G.A., 2000. Nonlinear Solid Mechanics Vol. 24 Wiley, Chichester.

Li, S., Wongsto, A., 2004. Unit cells for micromechanical analyses of particle-reinforced composites. Mech. Mater. 36 (7), 543–572. http://dx.doi.org/10.1016/S0167-6636(03)00062-0.

Michel, J.C., Moulinec, H., Suquet, P., 1999. Effective properties of composite materials with periodic microstructure: a computational approach. Comput. Methods Appl. Mech. Eng. 172 (1), 109–143. http://dx.doi.org/10.1016/S0045-7825(98)00227-8.

Nemat-Nasser, S., Hori, M., 1999. Micromechanics: Overall Properties of Heterogeneous Materials. Elsevier, North-Holland, Amsterdam.

Nguyen, V.P., Stroeven, M., Sluys, L.J., 2011. Multiscale continuous and discontinuous modeling of heterogeneous materials: a review on recent developments. J. Multiscale Model. 3 (04), 229–270. http://dx.doi.org/10.1142/S1756973711000509.

Nguyen, V.D., Wu, L., Noels, L., 2016. Unified treatment of microscopic boundary conditions and efficient algorithms for estimating tangent operators of the homogenized behavior in the computational homogenization method. Comput. Mech. 59 (3), 483–505. http://dx.doi.org/10.1007/s00466-016-1358-z.

Oller, S., Miquel-Canet, J., Zalamea, F., 2005. Composite material behavior using a homogenization double scale method. J. Eng. Mech. 131 (1), 65–79. http://dx.doi.org/10.1061/(ASCE)0733-9399(2005)131:1(65).

Piezel, B., Mercatoris, B.C.N., Trabelsi, W., Laiarinandrasana, L., Thionnet, A., Massart, T.J., 2012. Bending effect on the risk for delamination at the reinforcement/matrix interface of 3D woven fabric composite using a shell-like RVE. Compos. Struct. 94 (8), 2343–2357. http://dx.doi.org/10.1016/j.compstruct.2012.03.015.

Rasool, A., Böhm, H.J., 2012. Effects of particle shape on the macroscopic and microscopic linear behaviors of particle reinforced composites. Int. J. Eng. Sci. 58, 21–34. http://dx.doi.org/10.1016/j.ijengsci.2012.03.022.

Rudykh, S., deBotton, G., 2012. Instabilities of hyperelastic fiber composites: micromechanical versus numerical analyses. J. Elasticity 106 (2), 123–147. http://dx.doi.org/10.1007/s10659-011-9313-x.

Sun, C.T., Vaidya, R.S., 1996. Prediction of composite properties from a representative volume element. Compos. Sci. Technol. 56 (2), 171–179. http://dx.doi.org/10.1016/0266-3538(95)00141-7.

van Dijk, N.P., 2016. Formulation and implementation of stress-driven and/or strain-driven computational homogenization for finite strain. Int. J. Numer. Methods Eng. 107 (12), 1009–1028 10.1002/nme.5198.

Zahr-Viñuela, J., Pérez-Castellanos, J., 2011. Elastic constants and isotropy considerations for particulate metal–matrix composites. A multi-particle, cell-based approach. Compos. Part A: Appl. Sci. Manufact. 42 (5), 521–533. http://dx.doi.org/10.1016/j.compositesa.2011.01.011.